Investigation of Thermal Filamentation Instability over Gakona, Alaska
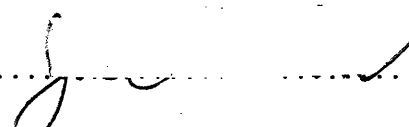
by

Joel Cohen

Submitted to the Department of Physics
in partial fulfillment of the requirements for the degree of
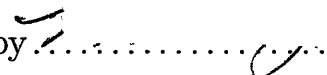
Bachelor of Science in Physics

at the

MASSACHUSETTS INSTITUTE OF TECHNOLOGY

May 2007
[June 2007]
Revised Thesis submitted June 13, 2007

Author . . . .
Department of Physics
June 13, 2007

Certified by . . . .
Min-Chang Lee
Head, Ionospheric Plasma Research Group
Plasma Science and Fusion Center
Thesis Supervisor

Certified by . . . .
Richard Temkin
Associate Director, Plasma Science and Fusion Center
Department of Physics
Thesis Supervisor

Accepted by . . . .
David Pritchard
Senior Thesis Coordinator, Department of Physics

Investigation of Thermal Filamentation Instability over Gakona, Alaska

by

Joel Cohen

Abstract

The thermal filamentation instability has been invoked to explain the formation of parallel plate waveguides in mid-latitude ionospheric plasmas during Arecibo, Puerto Rico heating experiments in 1997. The geometry of the kilometer-scale parallel plates predicted by thermal filamentation depends on the mode of the transmitted heater wave, as does the threshold to excite this instability. While plasma heating can excite small-scale irregularities via parametric instabilities, thermal filamentation is thought to produce large-scale irregularities. In Arecibo, the threshold for X-mode to induce irregularities was found to be greater than 1 V/m, while for O-mode it was on the order of mV/m. In recent plasma experiments in high-latitude ionospheric plasmas, carried out at the HAARP facility in Gakona, Alaska in summer 2005, spring 2006, and summer 2006, a weakening in ionogram traces was observed during O-mode and X-mode heating, leading to a scenario detailing the effects of thermal filamentation and short-scale irregularities caused by heating. The Gakona experiments using a high power HF heating facility and multiple diagnostic instruments shed light on the important role of the thermal filamentation instability in generating electromagnetic wave-induced plasma turbulence with a broad spectrum of wavelengths, ranging from meter to kilometer scales.

Acknowledgments

I have been blessed by family and many friends and mentors who have helped make my undergraduate experience successful. I thank my family for their support and many emails, both fun and encouraging.

I'm also grateful for a wonderful group of fellow students who are knowledgeable and fun to work with. Laura and Ania have been a pleasure to work with, and I have benefited from collaborating with them. Rezy has been an exemplary researcher and selfless fellow student, helping me many times to understand plasma physics concepts. I'm grateful for his friendship and mentoring. The HAARP operators provided excellent professional support and useful technical conversations. I would also like to thank my Thesis Co-supervisor, Dr. Richard Temkin.

Finally, I would not be where I am today without the unflagging support and mentoring of my Thesis Supervisor Prof. Min-Chang Lee. I'm thankful for his many hours of tutorial lectures, and more importantly his genuine concern for all of us.

Contents

List of Figures

Chapter 1

Introduction

The study of plasma physics ranges from the behavior of stars to controlled fusion, with diverse applications for energy, technology, and communication. I have been studying ionospheric electrodynamics, with a focus on instabilities and radio wave heating. The ionosphere has partially ionized gases known as ionospheric plasmas, which extend from about 90 km to $\sim$2000 km above the earth's surface, and this altitude range is divided into regimes based on density and phenomenology. The highest region, called the F-region, contains the peak plasma density, which usually occurs around 250-300 km. The study of ionospheric plasmas has applications for satellite communications, in addition to providing a natural laboratory to study complicated plasma processes.

The properties of the ionosphere can be altered by energetic charged particles, of solar origin or from cosmic rays, escaping from the radiation belts which extend several thousand kilometers above the earth's crust. The large population of high-energy charged particles in this region has implications for satellite integrity and astronaut safety. The particles that precipitate into the lower atmosphere can be diagnosed by their effects on ionospheric plasmas. Important information on radiation belts, such as particle density and energy, can then be inferred. Controlled study of radiation belts has been an active area of research. One approach is to transmit very low frequency (3-30 kHz) radio waves from the ground, which propagate into the radiation belts and cause particles to precipitate. Creation of artificial waveguides in

the ionosphere can facilitate the entering of these injected radio waves.

In this thesis I focus on the investigation of artificial waveguides created by high-power high-frequency (3-30 MHz) radio waves via a mechanism termed "the thermal filamentation instability." This instability leads to the excitation of large-scale plasma density irregularities that can behave as waveguides to direct or scatter radio waves. As partially ionized gases, ionospheric plasmas can respond to electric and magnetic fields. Naturally-occurring plasmas in the earth's atmosphere are always magnetized due to the earth's magnetic field. Such plasma thus has birefringent properties. For high-frequency (3-30 MHz) radio waves, the ordinary mode (O-mode) wave has an electric field that is parallel to the ambient magnetic field, while the extraordinary mode (X-mode) wave has an electric field that is perpendicular to the ambient magnetic field.

Note that for the O-mode wave the plasma appears to be unmagnetized, since the conductivity along the direction of the magnetic field is very large. Many plasma processes can occur naturally, or can be studied under controlled conditions with a radio-frequency (RF) heating facility. Such a facility has an array of antennae that transmit a beam of EM radiation into the ionosphere, heating the plasma and providing a source of energy for plasma instabilities or other phenomena. Depending on the experiment, the transmission may also be operated in continuous-wave (CW) or pulsed mode.

The thermal filamentation instability has been invoked to explain the formation of parallel-plate waveguides during RF heating experiments in Arecibo, Puerto Rico. In 1997, Lee et al observed the formation of sheet-like density irregularities aligned parallel to the meridional plane during CW O-mode heating [1]. These parallel plates were seen to move westward due to the $\mathbf{E} \times \mathbf{B}$ drift, a drift observed in plasma where the center of a charged particles's motion undergoes a constant drift with a velocity proportional to and a direction given by $\mathbf{E} \times \mathbf{B}$. Here $\mathbf{E}$ and $\mathbf{B}$ denote the ambient DC electric field and earth's magnetic field, respectively.

The geometry of the kilometer-scale parallel plates predicted by thermal filamentation depends on the mode of the transmitted heater wave, as does the threshold

wave electric field to excite this instability. While heating can excite small-scale (typically meter-scale) irregularities via parametric instabilities, thermal filamentation is thought to produce large-scale (typically hundred meter and kilometer-scale) irregularities [1]. In Arecibo, the threshold for X-mode to induce irregularities was found to be greater than 1 V/m, while for O-mode it was on the order of mV/m.

In our recent experiments at the High-frequency Active Auroral Research Program (HAARP) facility in Gakona, Alaska, carried out in summer 2005, spring 2006, and summer 2006, a weakening in ionogram traces was observed during O-mode and X-mode heating, leading to a scenario detailing the effects of thermal filamentation and short-scale irregularities caused by heating. An ionogram is the data returned by an instrument called a digital ionosonde, a swept-frequency HF radar that is used to diagnose ionospheric plasmas. Since there is a direct correspondence between plasma density and plasma frequency, these two parameters are used interchangeably. Our preliminary results from these experiments were presented at the Polar Aeronomy and Radio Science (PARS) Summer School ([2],[3]). The HAARP facility supports controlled experiments with an HF heater consisting of an array of crossed dipole antennas. We are able to transmit X-mode or O-mode heater waves with a frequency close to the maximum F-region plasma frequency (foF2).

The presentation of my thesis work is organized as follows. In Chapter 2, I describe the features of O- and X-mode radio waves transmitted from the ground as they reach their reflection heights in the F region of the ionosphere. The ionosphere is modeled as a uniform, cold plasma to a good approximation. In Chapter 3, I discuss how O- and X-mode radio waves can excite parallel-plate waveguide plasma structures in the F region via the thermal filamentation instability. Our experimental setup to investigate thermal filamentation instability, as well as measurements and data analysis, are presented in Chapter 4. Finally, in Chapter 5 a conclusion is drawn with discussions on future work.

Chapter 2

Cold Plasma Theory

2.1 Cold Plasma Dispersion Relation

2.1.1 Dielectric Tensor

Dispersion relations arise from the nontrivial solution of homogeneous field equations. In Maxwell's equations we must find $\mathbf{j}=\mathbf{j}(\mathbf{E})$. This could be done using a conductivity tensor $\boldsymbol{\sigma}$, or by thinking of $\mathbf{j}$ as a displacement current in a dielectric, and using a dielectric tensor $\boldsymbol{\epsilon}$. The dielectric tensor has an additive nature, which is captured by introducing the susceptibility. This quantity gives each species contribution to the dielectric tensor [4].

We assume a uniform, time-invariant background plasma and introduce perturbations with a sinusoidal, steady-state form proportional to $e^{i(\mathbf{k}\cdot\mathbf{r}-\omega t)}$. We begin with Ampere's law from Maxwell's equations with the current term included:

$$\nabla \times \mathbf{B} = \frac{4\pi}{c}\mathbf{j} + \frac{1}{c}\frac{\partial \mathbf{E}}{\partial t} = \frac{1}{c}\frac{\partial \mathbf{D}}{\partial t} \tag{2.1}$$

Fourier transforming this equation (equivalent to substituting our perturbation forms and eliminating the time dependence) yields an algebraic expression in ω-$\mathbf{k}$ space

instead of **r**-t space.

$$-i\omega \mathbf{D}(\omega, \mathbf{k}) = -i\omega \mathbf{E}(\omega, \mathbf{k}) + 4\pi \mathbf{j}(\omega, \mathbf{k}) \tag{2.2}$$

$$\mathbf{D}(\omega, \mathbf{k}) = \mathbf{E}(\omega, \mathbf{k}) + \frac{4\pi i}{\omega} \mathbf{j}(\omega, \mathbf{k}) \tag{2.3}$$

$$= \epsilon(\omega, \mathbf{k}) \cdot \mathbf{E}(\omega, \mathbf{k}) \tag{2.4}$$

The current itself is given by a sum over the velocities of each species:

$$\mathbf{j} = \sum_s \mathbf{j}_s = \sum_s n_s q_s \mathbf{v}_s \tag{2.5}$$

Introducing the susceptibility, we can write:

$$\epsilon(\omega, \mathbf{k}) = 1 + \sum_s \chi_s(\omega, \mathbf{k}) \tag{2.6}$$

Substituting these expressions for **j** and ϵ back into our expression for **D** above, we find

$$\sum_s \chi_s(\omega, \mathbf{k}) \cdot \mathbf{E} = \frac{4\pi i}{\omega} \sum_s \mathbf{j}_s(\omega, \mathbf{k}) \tag{2.7}$$

and we can now write

$$\mathbf{j}_s = -\frac{i\omega}{4\pi} \chi_s \cdot \mathbf{E} \tag{2.8}$$

We now consider the fluid equation of motion for one species. Because we are considering a cold plasma, viscosity can be neglected and no shear forces will be present. Then the only forces are due to the Lorentz force.

$$n_s m_s \frac{d\mathbf{v}_s}{dt} = n_s q_s \left(\mathbf{E} + \frac{\mathbf{v}_s}{c} \times \mathbf{B} \right) \tag{2.9}$$

Note that the number density drops out. Expanding the total derivative, we have

$$m_s \left(\frac{\partial}{\partial t} + \mathbf{v}_s \cdot \nabla \right) \mathbf{v}_s = q_s \left(\mathbf{E} + \frac{\mathbf{v}_s}{c} \times \mathbf{B} \right) \tag{2.10}$$

We assume that n_s and $\mathbf{B} = B_0 \hat{\mathbf{z}}$ are finite, uniform, and time-invariant to zero order.

Furthermore, $\mathbf{v}_s = \mathbf{j}_s = \mathbf{E} = 0$. After Fourier transforming,

$$-i\omega m_s \mathbf{v}_s = q_s \left(\mathbf{E} + \frac{\mathbf{v}_s}{c} \times \mathbf{B} \right) \tag{2.11}$$

We now solve this equation for the components of $\mathbf{v}_s$. For simplicity, we assume general forms for $\mathbf{v}_s$ and $\mathbf{E}$ in three dimensions but take $\mathbf{B} = B_0 \hat{\mathbf{z}}$. Our equation becomes

$$-i\omega m_s \begin{pmatrix} v_x \\ v_y \\ v_z \end{pmatrix} = q_s \left[\begin{pmatrix} E_x \\ E_y \\ E_z \end{pmatrix} + \frac{B_0}{c} \begin{pmatrix} v_y \\ -v_x \\ 0 \end{pmatrix} \right] \tag{2.12}$$

This gives three equations in the three unknowns v_x, v_y, v_z:

$$-i\omega m_s v_x = q_s E_x + \frac{B_0}{c} v_y q_s \tag{2.13a}$$

$$-i\omega m_s v_y = q_s E_y - \frac{B_0}{c} v_x q_s \tag{2.13b}$$

$$-i\omega m_s v_z = q_s E_z \tag{2.13c}$$

Solving the second equation for v_y yields

$$v_y = \frac{iq_s}{\omega m_s} \left(E_y - \frac{B_0}{c} v_x \right) \tag{2.14}$$

Substituting into the first equation and rearranging yields

$$v_x = \frac{\frac{q_s \omega}{m_s} \left(iE_x - \frac{\omega_{cs}}{\omega} E_y \right)}{\omega^2 - \omega_{cs}^2} \tag{2.15}$$

Similarly we obtain

$$v_y = \frac{\frac{q_s \omega}{m_s} \left(\frac{\omega_{cs}}{\omega} E_x + iE_y \right)}{\omega^2 - \omega_{cs}^2} \tag{2.16}$$

And finally

$$v_z = \frac{iq_s}{\omega m_s} E_z \tag{2.17}$$

Recall our two expressions for $\mathbf{j}_s$:

$$n_s q_s \mathbf{V}_s = \mathbf{j}_s = -\frac{i\omega}{4\pi} \boldsymbol{\chi}_s \cdot \mathbf{E} \tag{2.18}$$

Breaking this equation into components and rearranging we find

$$v_{si} = -\frac{i\omega}{4\pi n_s q_s} \sum_j \chi_{ij} E_j \tag{2.19}$$

If we look at the expressions for the components of $\mathbf{v}_s$, we can define coefficients α_{ij} such that

$$v_{si} = \sum_j \alpha_{ij} Ej \tag{2.20}$$

Then the components of the susceptibility tensor can be found:

$$\chi_{ij} = \frac{4\pi i n_s q_s}{\omega} \alpha_{ij} = \frac{\omega_{ps}^2}{\omega} \frac{i m_s}{q_s} \alpha_{ij} \tag{2.21}$$

Where $\omega_{ps}^2 = \frac{4\pi n_s q_s^2}{m_s}$ is the plasma frequency. Looking at our expressions for v_x, v_y, and v_z we see that

$$\chi_{xx} = \chi_{yy} = -\frac{1}{2} \sum_s \frac{\omega_{ps}^2}{\omega^2} \left[\frac{\omega}{\omega + \omega_{cs}} + \frac{\omega}{\omega - \omega_{cs}} \right] \tag{2.22}$$

$$\chi_{xy} = -\chi_{yx} = -\frac{i}{2} \sum_s \frac{\omega_{ps}^2}{\omega^2} \left[\frac{\omega}{\omega + \omega_{cs}} + \frac{\omega}{\omega - \omega_{cs}} \right] \tag{2.23}$$

Now we will rewrite the coefficients. It will be convenient to define factors containing the various frequencies—this will also allow easy factoring of the cold plasma

dispersion relation. Recall that $\epsilon = 1 + \chi$. Let

$$R = 1 - \sum_s \frac{\omega_{ps}^2}{\omega^2} \frac{\omega}{\omega + \omega_{cs}} \tag{2.24}$$

$$L = 1 - \sum_s \frac{\omega_{ps}^2}{\omega^2} \frac{\omega}{\omega - \omega_{cs}} \tag{2.25}$$

$$P = 1 - \sum_s \frac{\omega_{ps}^2}{\omega^2} \tag{2.26}$$

Then we see that

$$1 + \chi_{s,xx} = 1 + \chi_{s,yy} = \frac{1}{2}(R + L) \tag{2.27}$$

$$\chi_{s,xy} = -\chi_{s,yx} = -\frac{i}{2}(R - L) \tag{2.28}$$

Then we can define two more quantities $S = \frac{1}{2}(R + L)$ and $D = \frac{1}{2}(R - L)$. Finally we can write the dielectric tensor:

$$\epsilon = \begin{pmatrix} S & -iD & 0 \\ iD & S & 0 \\ 0 & 0 & P \end{pmatrix} \tag{2.29}$$

2.1.2 Plane Waves

We will now solve Maxwell's equations to find plane wave solutions in plasma. We begin with Faraday's law and the generalized Ampere's law:

$$\nabla \times \mathbf{B} = \frac{4\pi \mathbf{j}}{c} + \frac{1}{c}\frac{\partial \mathbf{E}}{\partial t} = \frac{1}{c}\frac{\partial \mathbf{D}}{\partial t} \tag{2.30}$$

$$\nabla \times \mathbf{E} = -\frac{1}{c}\frac{\partial \mathbf{B}}{\partial t} \tag{2.31}$$

19

Fourier analyzing in space and time and rearranging, we find

$$\mathbf{k} \times \mathbf{B} = -\frac{\omega}{c}\mathbf{D} \tag{2.32}$$

$$\mathbf{k} \times \mathbf{E} = \frac{\omega}{c}\mathbf{B} \tag{2.33}$$

$$\tag{2.34}$$

We cross $\mathbf{k}$ into the second equation and substitute from the first equation.

$$\mathbf{k} \times (\mathbf{k} \times \mathbf{E}) = \frac{\omega}{c}\mathbf{k} \times \mathbf{B} = -\frac{\omega^2}{c^2}\mathbf{D} \tag{2.35}$$

Recalling our expression for $\mathbf{D}$ above we arrive at the wave equation:

$$\mathbf{k} \times (\mathbf{k} \times \mathbf{E}) + \frac{\omega^2}{c^2}\boldsymbol{\epsilon} \cdot \mathbf{E} = 0 \tag{2.36}$$

It is convenient to introduce a wave normal vector, defined as

$$\mathbf{n} = \frac{\mathbf{k}c}{\omega} \tag{2.37}$$

Then our wave equation is transformed into

$$\mathbf{n} \times (\mathbf{n} \times \mathbf{E}) + \boldsymbol{\epsilon} \cdot \mathbf{E} = 0 \tag{2.38}$$

For convenience, and without loss of generality, we will take $\mathbf{B} = B_0\hat{\mathbf{z}}$ and restrict the wave normal so $\mathbf{n} = n_x\hat{\mathbf{x}} + n_y\hat{\mathbf{y}}$. If θ is the angle between $\mathbf{B}$ and $\mathbf{n}$, then

$$\mathbf{n} \times (\mathbf{n} \times \mathbf{E}) = n^2 \begin{pmatrix} -\cos^2\theta & 0 & \cos\theta\sin\theta \\ 0 & 1 & 0 \\ \cos\theta\sin\theta & 0 & -\sin^2\theta \end{pmatrix} \begin{pmatrix} E_x \\ E_y \\ E_z \end{pmatrix} \tag{2.39}$$

If we use this form in the equation above, we can easily get an equation of the form $\mathbf{A} \cdot \mathbf{E} = 0$, where $\mathbf{A}$ is a second-rank tensor. The condition for solubility is that the

determinant of **A** is zero.

$$\begin{vmatrix} S - n^2\cos^2\theta & -iD & n^2\cos\theta\sin\theta \\ iD & S - n^2 & 0 \\ n^2\cos\theta\sin\theta & 0 & P - n^2\sin^2\theta \end{vmatrix} = 0 \qquad (2.40)$$

Evaluating the determinant and substituting $S^2 - D^2 = RL$ yields:

$$RLP - RLn^2\sin^2\theta - SPn^2 + Sn^4\sin^2\theta - SPn^2\cos^2\theta + Pn^4\cos^2\theta = 0 \qquad (2.41)$$

Substituting sin in favor of cos and grouping terms,

$$RLP - 2SPn^2 + Pn^4 = \sin^2\theta \left[RLn^2 - Sn^4 - SPn^2 + Pn^4 \right] \qquad (2.42)$$

Similarly, substituting cos in favor of sin and grouping terms,

$$RLP - RLn^2 - SPn^2 + Sn^4 = -\cos^2\theta \left[RLn^2 - Sn^4 - SPn^2 + Pn^4 \right] \qquad (2.43)$$

And finally we combine these two expressions, noting that $2S = (R + L)$.

$$\tan^2\theta = -\frac{P(n^2 - R)(n^2 - L)}{(Sn^2 - RL)(n^2 - P)} \qquad (2.44)$$

This is then the general dispersion relation for waves in a cold plasma. It can be used to do ray tracing in a model ionosphere, in which form it is called the Appleton-Hartrey relation. By choosing particular values of θ, we can also recover the various normal modes supported by a cold plasma. For example, the existence of a magnetic field makes a plasma a birefringent medium, and the particular values $\theta = 0$ and $\theta = pi/2$ yield the X (extraordinary) and O (ordinary) modes. The choice $\theta = 0$ yields $n^2 = R$ and $n^2 = L$. These are the two branches of the so-called X-mode that occur when **E** $\perp$ **B**. For the choice $\theta = pi/2$, $n^2 = RL/S$ and $n^2 = P$. This implies that when **E** is parallel or anti-parallel to **B**, an electromagnetic wave may either excite an electrostatic oscillation (Langmuir wave) or exist as the O-mode. Waves transmitted

from the ground will undergo refraction in the ionosphere, and near the reflection height will have $\mathbf{k} \parallel \mathbf{B}$ for X-mode and $\mathbf{E} \perp \mathbf{B}$ for O-mode.

Chapter 3

Thermal Filamentation

3.1 Ponderomotive and Thermal Pressure Forces

The thermal pressure force provides the nonlinearity for the mechanism forming parallel-plate waveguides in the ionosphere [5]. We consider the combined effect of two HF electrostatic waves. We take the electric fields to be as follows.

$$\mathbf{E} = E \frac{\mathbf{k}}{k} e^{i(\omega t - \mathbf{k} \cdot \mathbf{r})} \tag{3.1}$$

The equation of motion for an electron in one of these fields is just $m\ddot{\mathbf{x}} = -e\mathbf{E}$, and then we substitute a perturbation form for $\mathbf{x}$.

$$\mathbf{x} = \frac{eE}{m\omega^2} \frac{\mathbf{k}}{k} \cos(\omega t - \mathbf{k} \cdot \mathbf{r}) \tag{3.2}$$

To derive the effect of the ponderomotive force, we calculate the effect of each field on electrons and then self-consistently superimpose the two fields. The thermal pressure force is derived by considering differential heating by the two waves. We arrive at the expressions for the forces on electrons due to the wave electric fields:

$$\mathbf{F}_1 = -eE_1 \frac{\mathbf{k_1}}{k_1} \cos(\omega_1 t - \mathbf{k_1} \cdot (\mathbf{r} + \mathbf{x_2})) \tag{3.3}$$

$$\mathbf{F}_2 = -eE_2 \frac{\mathbf{k_2}}{k_2} \cos(\omega_2 t - \mathbf{k_2} \cdot (\mathbf{r} + \mathbf{x_1})) \tag{3.4}$$

Taylor expanding, we get the following expressions including zeroth and first order:

$$\mathbf{F_1} \approx \; - \; eE_1\frac{\mathbf{k_1}}{k_1}\cos\left(\omega_1 t - \mathbf{k_1}\cdot\mathbf{r}\right)$$

$$+ \; \frac{e^2 E_1 E_2}{m\omega^2}\frac{\mathbf{k_1}(\mathbf{k_1}\cdot\mathbf{k_2})}{k_1 k_2}\sin\left(\omega_1 t - \mathbf{k_1}\cdot\mathbf{r}\right)\cos\left(\omega_2 t - \mathbf{k_2}\cdot\mathbf{r}\right) \qquad (3.5\text{a})$$

$$\mathbf{F_2} \approx \; - \; eE_2\frac{\mathbf{k_2}}{k_2}\cos\left(\omega_2 t - \mathbf{k_2}\cdot\mathbf{r}\right)$$

$$+ \; \frac{e^2 E_1 E_2}{m\omega^2}\frac{\mathbf{k_2}(\mathbf{k_1}\cdot\mathbf{k_2})}{k_1 k_2}\sin\left(\omega_2 t - \mathbf{k_2}\cdot\mathbf{r}\right)\cos\left(\omega_1 t - \mathbf{k_1}\cdot\mathbf{r}\right) \qquad (3.5\text{b})$$

Now we combine the two forces, discarding the zeroth order terms to arrive at nonlinear forces due to the interference of the HF waves. This is done by taking the sum and difference of the first order terms. For example, if we use trigonometric identities on the first order terms we obtain:

$$\mathbf{F_{N1}} = \frac{e^2 E_1 E_2}{m\omega^2}\frac{\mathbf{k_1}(\mathbf{k_1}\cdot\mathbf{k_2})}{k_1 k_2}\Big[\sin\left((\omega_1 + \omega_2)t - (\mathbf{k_1} + \mathbf{k_2})\cdot\mathbf{r}\right)$$

$$+ \sin\left((\omega_1 - \omega_2)t - (\mathbf{k_1} - \mathbf{k_2})\cdot\mathbf{r}\right)\Big] \qquad (3.6\text{a})$$

$$\mathbf{F_{N2}} = \frac{e^2 E_1 E_2}{m\omega^2}\frac{\mathbf{k_2}(\mathbf{k_1}\cdot\mathbf{k_2})}{k_1 k_2}\Big[\sin\left((\omega_1 + \omega_2)t - (\mathbf{k_1} + \mathbf{k_2})\cdot\mathbf{r}\right)$$

$$- \sin\left((\omega_1 - \omega_2)t - (\mathbf{k_1} - \mathbf{k_2})\cdot\mathbf{r}\right)\Big] \qquad (3.6\text{b})$$

Taking the second sine function in each expression and adding, we obtain:

$$\mathbf{F_{NID}} = \frac{e^2 E_1 E_2}{m\omega^2}\frac{\mathbf{k_1}(\mathbf{k_1}\cdot\mathbf{k_2})}{k_1 k_2}\sin\left((\omega_1 - \omega_2)t - (\mathbf{k_1} - \mathbf{k_2})\cdot\mathbf{r}\right)$$

$$- \frac{e^2 E_1 E_2}{m\omega^2}\frac{\mathbf{k_2}(\mathbf{k_1}\cdot\mathbf{k_2})}{k_1 k_2}\sin\left((\omega_1 - \omega_2)t - (\mathbf{k_1} - \mathbf{k_2})\cdot\mathbf{r}\right) \qquad (3.7)$$

and when $\omega_1 \approx \omega_2 \approx \omega_{pe}$, then

$$\mathbf{F_{NID}} \approx \frac{e^2 E_1 E_2}{m\omega^2}\frac{(\mathbf{k_1}\cdot\mathbf{k_2})}{k_1 k_2}(\mathbf{k_1} - \mathbf{k_2})\sin\left((\omega_1 - \omega_2)t - (\mathbf{k_1} - \mathbf{k_2})\cdot\mathbf{r}\right) \qquad (3.8)$$

Then we find an apparent electric field for the nonlinear ponderomotive force.

$$\mathbf{E_{app,N}} = \frac{k_B \epsilon \nu_{ei} E_1 E_2}{e\sigma_h k_\parallel^2}(\mathbf{k_1} - \mathbf{k_2})\sin\left((\omega_1 - \omega_2)t - (\mathbf{k_1} - \mathbf{k_2})\cdot\mathbf{r}\right) \qquad (3.9)$$

The thermal pressure force is treated by again beginning with two HF electrostatic waves with wave electric fields as given in Equation 3.1. We want to find the collisional dissipation defined by

$$d = \epsilon_0 \nu_{ei} \langle (\mathbf{E_1} + \mathbf{E_2})^2 \rangle \tag{3.10}$$

Note that $\langle (\mathbf{E_1} + \mathbf{E_2})^2 \rangle = \langle |\mathbf{E_1}|^2 + |\mathbf{E_2}|^2 + 2\mathbf{E_1} \cdot \mathbf{E_2}^* \rangle$. The first two terms are constants, and the third term gives the wave interference:

$$d = \epsilon_0 \nu_{ei} \langle 2E_1 E_2 \Big(\frac{\mathbf{k_1} \cdot \mathbf{k_2}}{k_1 k_2} \Big) \cos \left((\omega_1 - \omega_2)t - (\mathbf{k_1} - \mathbf{k_2}) \cdot \mathbf{r} \right) \rangle \tag{3.11}$$

Note that the frequency of the cosine term $(\omega_1 - \omega_2) \ll \omega_{pe}$. We also now assume $|\mathbf{k_1}| \approx |\mathbf{k_2}|$, and if $\mathbf{k_1} \parallel \mathbf{k_2}$ then we obtain the following:

$$d = \epsilon_0 \nu_{ei} E_1 E_2 \cos \left((\omega_1 - \omega_2)t - (\mathbf{k_1} - \mathbf{k_2}) \cdot \mathbf{r} \right) \tag{3.12}$$

The mean collisional dissipation leads to an electron temperature perturbation δT_e. In partially ionized plasmas, we have several collision frequencies, such as the electron-ion (ν_{ei}), electron-neutral (ν_{en}), and ion-neutral (ν_{in}) collisional frequencies. We are concerned with F-region plasmas, where the dominant species is O^+. The electron-ion collision frequency here is about 500 Hz - 1 kHz, and $\nu_{en} \ll \nu_{ei}$. We will assume that no heat is transferred from the electrons to either ions or neutrals, so that δT_e depends only on the electron heat conduction, denoted σ_h. Finally, we assume that the differential dissipation is exactly balanced by heat conduction. We consider heat conduction and collisional dissipation along the direction of the magnetic field $\mathbf{B} = B_0 \hat{z}$.

$$-\frac{\partial}{\partial z} \left[\sigma_h \frac{\partial}{\partial z} (\delta T_e) \right] = \epsilon_0 \nu_{ei} E_1 E_2 \cos \left((\omega_1 - \omega_2)t - (\mathbf{k_1} - \mathbf{k_2}) \cdot \mathbf{r} \right) \tag{3.13}$$

Then, using $k_\parallel = (\mathbf{k_1} - \mathbf{k_2})_z$, we integrate to find

$$\delta T_e = \frac{\epsilon_0 \nu_{ei} E_1 E_2}{\sigma_h k_\parallel^2} \cos \left((\omega_1 - \omega_2)t - (\mathbf{k_1} - \mathbf{k_2}) \cdot \mathbf{r} \right) \tag{3.14}$$

25

Now we can solve for the thermal pressure force $\mathbf{F_{th}} = -\nabla(n_0 k_B \delta T_e)$. Then we find the corresponding apparent electric field as $\mathbf{E_{app,th}} = \mathbf{F_{th}}/(-en_0)$.

$$\mathbf{E_{app,th}} = \frac{k_B \epsilon_0 \nu_{ei} E_1 E_2}{e \sigma_h k_\parallel^2}(\mathbf{k_1} - \mathbf{k_2}) \sin\left((\omega_1 - \omega_2)t - (\mathbf{k_1} - \mathbf{k_2}) \cdot \mathbf{r}\right) \qquad (3.15)$$

Comparing this to our apparent electric field from the ponderomotive force above, we find that for equivalent electric fields,

$$k_\parallel = \left(\frac{2n_0 \nu_{ei} k_B}{\sigma_h}\right)^{\frac{1}{2}} \qquad (3.16)$$

We take the following values for our parameters: $n_0 = 4.5 \times 10^{11} \text{m}^{-3}$, $\sigma_h = 2.4 \times 10^{-4} \text{J}/(\text{m} \cdot \text{s} \cdot \text{K})$, $k_B = 1.38 \times 10^{-23} \text{J/K}$, and $\nu_{ei} \approx 500 \text{Hz}$. Then we find that

$$k_\parallel = 5.6 \times 10^{-3} \text{m}^{-1} \qquad (3.17)$$

$$\lambda_\parallel \approx 1 \text{km} \qquad (3.18)$$

Thus for the thermal pressure force to dominate over the ponderomotive force, the scale length of the irregularities must be kilometer-scale.

3.2 Thermal Filamentation Scenario

Given appropriate conditions, we expect the thermal pressure force to create parallel-plate waveguides in the ionosphere. The primary means of detecting these at Gakona to date has been a swept-frequency HF radar called an ionosonde. The URSI handbook on ionograms mentions one possible mechanism causing a rapid loss in ionogram signal. Ion acoustic waves related to plasma instabilities can cause incoherent reflection and thus a very weak returned signal [6]. We expect that during heating small scale irregularities may scatter ionosonde signals and cause a loss in received signal near the heater frequency. A second possible heater effect is the excitation of thermal filamentation instability, which we believe can reduce returns of northward signals.

Figure 3-1 shows the geometry of O-mode and X-mode heater waves' electric,
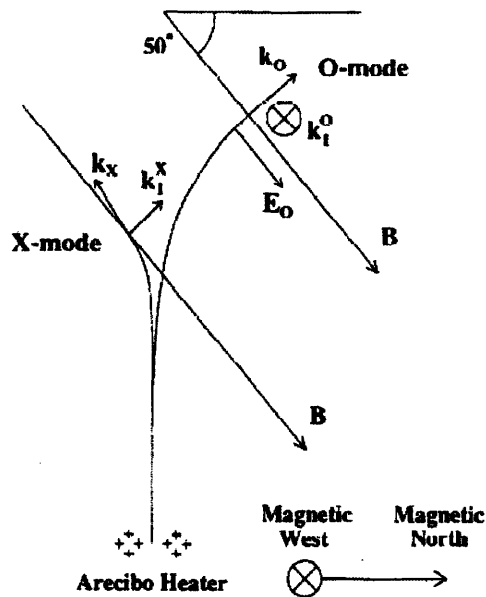
Figure 3-1: Ray paths of O-mode and X-mode heater waves [1].

magnetic, and wave vectors at their reflection heights. The O-mode heater wave aligns with its electric field along **B**, so the plasma acts as if it were unmagnetized. The heater wave will produce density perturbations with a wave vector perpendicular to the meridional plane, as shown by k_1^O. In contrast, the X-mode heater wave aligns with its electric field perpendicular to **B**, so the perturbations it produces have a wave vector perpendicular to **B**, as shown by k_1^X.

As shown in Figure 3-2, then, CW O-mode heating produces sheet-like irregularities parallel to the meridional plane. Ionosonde signals that are refracted by the ionosphere may reach and be reflected by the density gradient created by the plasma blob. These reflected signals reaching the ionosonde are seen as blue northward traces. As shown in Figure 3-3 CW X-mode heating produces sheet-like irregularities that are perpendicular to the meridional plane. In this scenario, the ionosonde signals that would otherwise be reflected by the plasma blob are ducted away or undergo scattering. Thus we suggest that anomalous absorption of the ionosonde signals is caused by heater and thermal-filamentation induced irregularities.
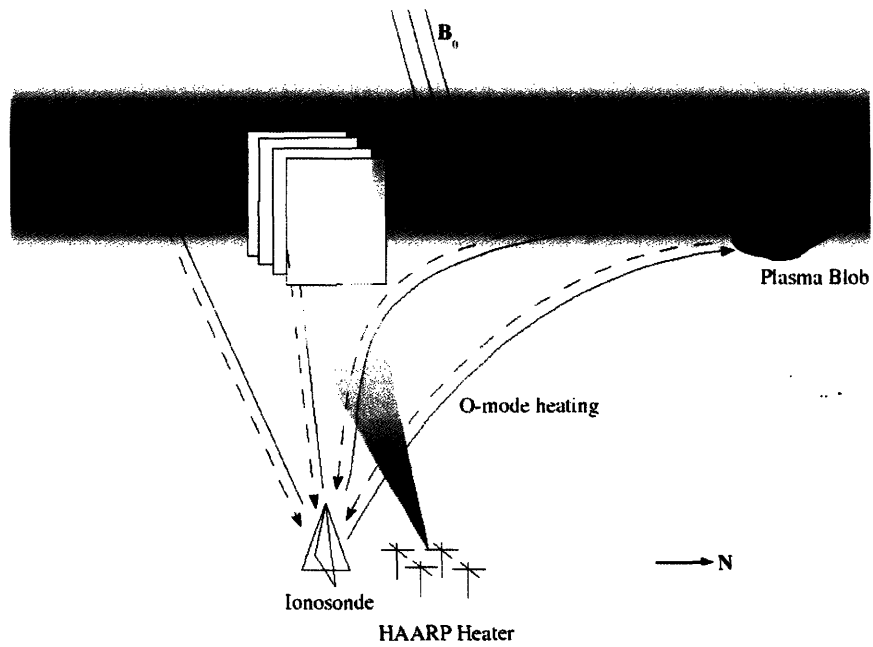
27

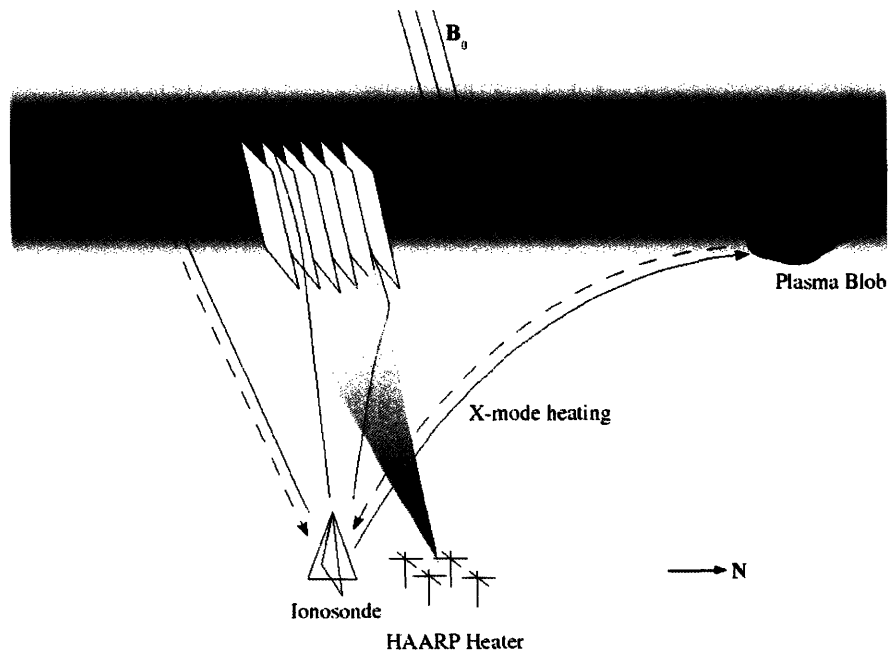Figure 3-2: Geometry and proposed scenario of O-mode induced irregularities.

Figure 3-3: Geometry and proposed scenario of X-mode induced irregularities.

Chapter 4

Data and Interpretation

4.1 Experimental Setup

We have conducted several experimental campaigns at the HAARP facility in Gakona, Alaska. Here we focus on datasets from summer 2005 and summer 2006, acquired during the Polar Aeronomy and Radio Science (PARS) Summer School, and from a campaign during spring 2006. Our primary diagnostic is a digital ionosonde, which is a swept-frequency HF radar that may operate from 1-20 MHz. The ionosonde steps through a preset range of frequencies, sending out both O-mode and X-mode signals, and waiting a short time to receive any returned signal. The primary data returned by the ionosonde is then a plot of returned signal on a virtual height versus frequency plot. The signal is assumed to travel at the speed of light in vacuum, so virtual height is found directly from the time lag between signal transmission and reception. The radar itself has an array of seven antennas, allowing seven distinct beam directions, so some degree of horizontal spatial information can be collected.

Since the sky never darkened completely during our experiments, we were unable to use an All Sky Imager to monitor optical emissions, in order to image the parallel-plate waveguides. Satellite scintillation measurements, another diagnostic useful for gathering spatial information, were also not available. Other complimentary instruments included a GPS receiver to calculate TEC, a riometer, and a magnetometer. The GPS receiver monitors signals from several GPS satellites, and the signal provides

2005Aug21; 1511 - 1529 UT; South to North
Meridian Time ~UT-10 hrs

Altitude (km)

1000

800

600

400

200

0

56   59   62   65   68   71   74   77

Gak   PtY   Kak

$N_e (10^{11} el/cm^3)$

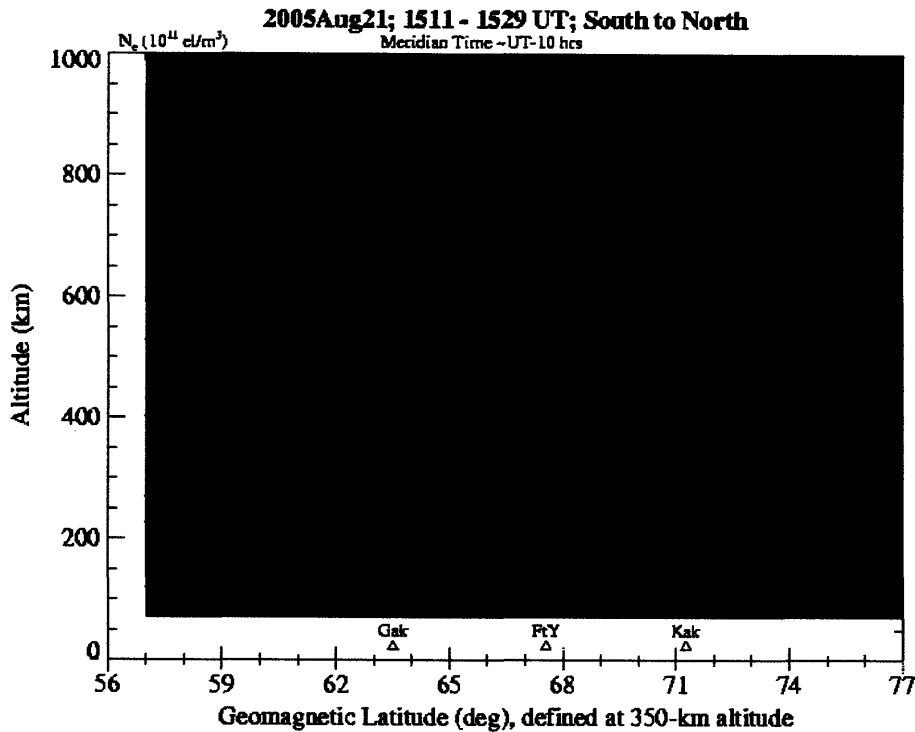Geomagnetic Latitude (deg), defined at 350-km altitude

Figure 4-1: TEC measurements from GPS satellites over Alaska

a measure of the height-integrated plasma content (TEC) of the ionosphere. Several satellites moving over Alaska allow the plotting of TEC contours, which can indicate large-scale plasma irregularities such as blobs. The riometer monitors absorption, which may significantly increase due to proton precipitation or the presence of the electrojet. The riometer monitors 30 MHz noise, the majority of which comes from outside the ionosphere. Over time, a quiet day curve is generated which the signal at a particular time can be compared to. When absorption is high, the ionosonde signals cannot penetrate effectively into the F-region, so ionogram data is not an accurate measure of F-region processes. It is also problematic if the absorption fluctuates significantly in a short period of time. Finally, the magnetometer provides a measure of electrojet activity, essentially measuring the induced current on the ground due to changes in the E-region electrojet current.

4.2 Summer 2005

We conducted experiments on August 21, 2005 from 10:00 UT until 12:15 UT. This night was particularly interesting due to the presence of a plasma blob to the north of HAARP. Figure 4-1 shows TEC measurements that indicate a large region of high density to the north. Ionosonde signals transmitted at large angles with respect to the zenith will be refracted as they propagate, and have a chance to be reflected by the blob and return to the ionosonde. These signals are coded blue in the ionograms.

Several representative ionograms from this period are shown in Figure 4-2. Prior to our experiments, another group was transmitting ramped X-mode vertically, and ionograms showed strong spread-F as well as signals from the northward direction (a). Our experiments began with 3.16 MHz CW O-mode transmitted along magnetic zenith. As soon as the heater was switched to this mode, a vertical stripe appeared around the heater frequency, affecting the blue northward traces (b). This reduction in signal persisted throughout the O-mode heating. When the heater was turned off, the traces filled in again (c).

When the heater was turned on at 11:05:30, transmitting 3.15 MHz CW X-mode vertically, a decrease in northward signal intensity was again seen, but was more pronounced this time (d). Changing the heater direction to magnetic zenith did not make an appreciable difference (e), but increasing the heater frequency to 4.50 MHz at 11:35:30 altered the appearance of the ionograms. As seen in (f), a vertical stripe appeared around the new heater frequency, but was narrower and bore greater resemblance to the first O-mode stripe in (b), centered in a narrow frequency range around the heater frequency. At this higher frequency, there was not a significant difference when we switched to CW O-mode, still transmitting at 4.50 MHz (g). Increasing the frequency once more and transmitting 6.80 MHz CW O-mode had no apparent effect on the ionogram traces and they filled in again quickly (h). When the heater was turned off, the traces remained essentially the same (i).

There was also an apparent weakening of the X-mode trace on the ionograms when the heater began transmitting CW X-mode (d), and in fact this trace disappeared
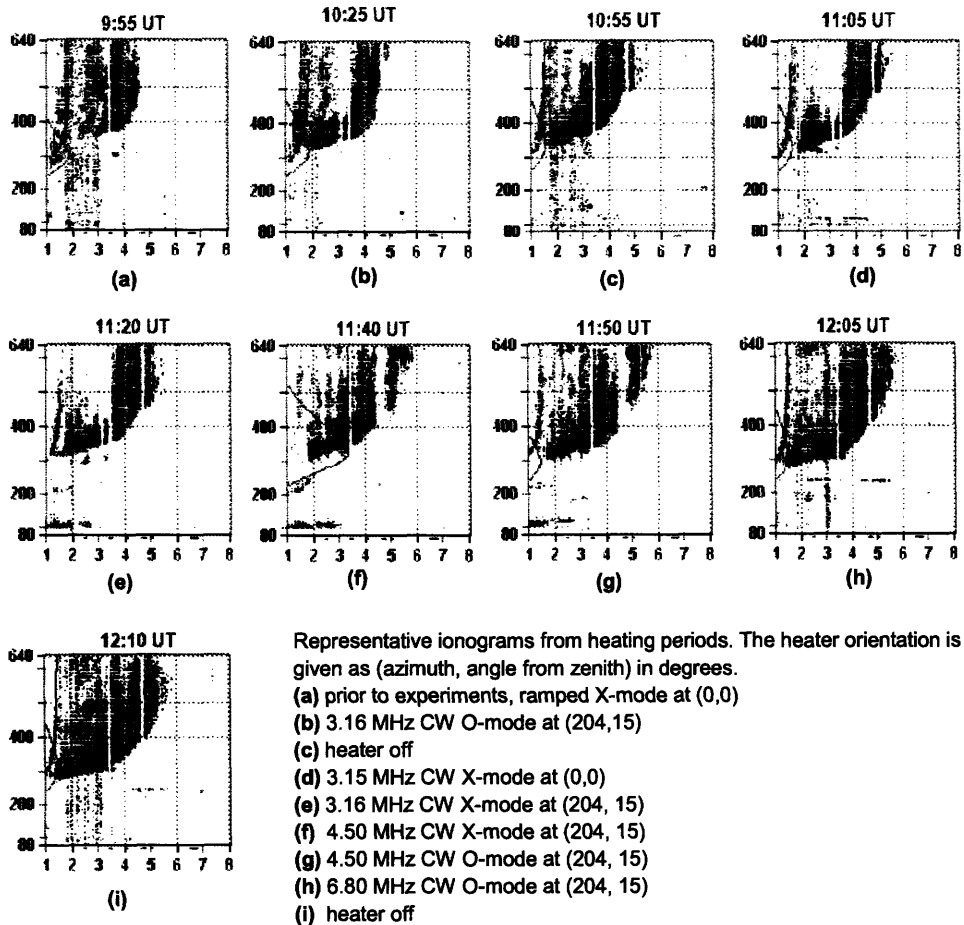
Representative ionograms from heating periods. The heater orientation is given as (azimuth, angle from zenith) in degrees.
(a) prior to experiments, ramped X-mode at (0,0)
(b) 3.16 MHz CW O-mode at (204,15)
(c) heater off
(d) 3.15 MHz CW X-mode at (0,0)
(e) 3.16 MHz CW X-mode at (204, 15)
(f) 4.50 MHz CW X-mode at (204, 15)
(g) 4.50 MHz CW O-mode at (204, 15)
(h) 6.80 MHz CW O-mode at (204, 15)
(i) heater off

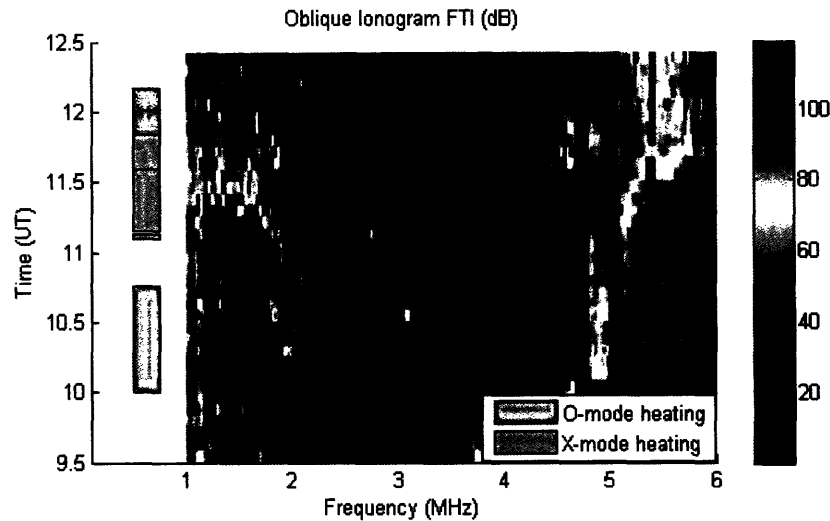Figure 4-2: Ionograms from August 21, 2005. Times are in UT.

Figure 4-3: Frequency-Time-Intensity plot of ionosonde signals on August 21, 2005

altogether after 5 minutes. However, when the heater was later switched to CW O-mode (g,h) and eventually turned off (i), the X-mode trace did become apparent again, so it is questionable whether the heater had an effect on the X-mode trace.

4.2.1 Ionogram Analysis

To analyze the effect of heater-induced irregularities on the ionosonde signals, we looked in detail at each return recorded by the ionosonde. Every point in the ionogram is a return from a particular frequency, and carries polarization, beam direction, range, and amplitude information. For each frequency bin, a Most Probable Amplitude (MPA) is calculated and used as a noise threshold. All returns with an amplitude greater than 6 dB above the MPA are plotted on the ionogram.

Taking the entire set of ionograms from this night's experiment, we were able to create a Frequency-Time-Intensity (FTI) plot, shown in Figure 4-3. This shows how the strength of the height-integrated signal at each frequency varies throughout the course of the experiment. Blue-shaded regions on the left indicate O-mode heating, while orange-shaded regions indicate X-mode heating. Note the dramatically reduced signal during the first three heating periods, in the frequency range 3.1-3.3 MHz.
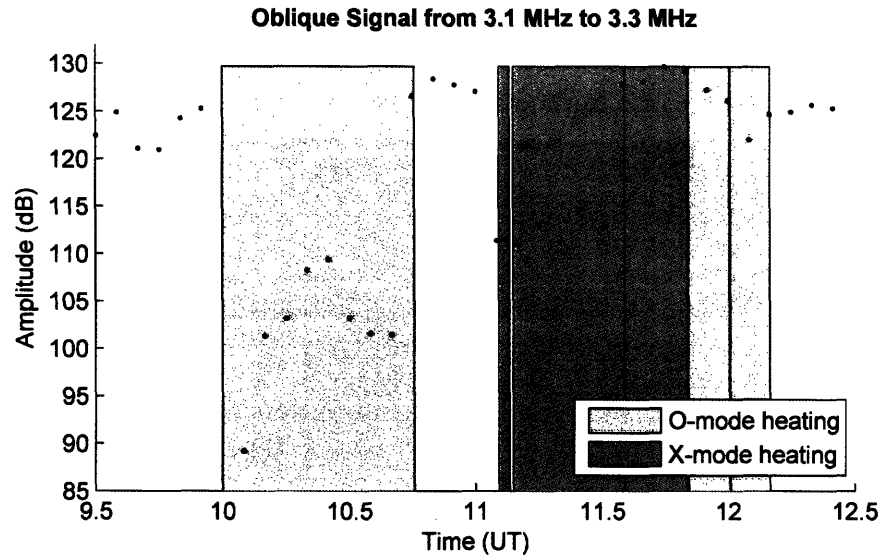
33

Figure 4-4: Ionosonde signals in the range 3.1-3.3 MHz on August 21, 2005

Smaller reductions in signal are also seen in the whole range between 2.5 and 3.5 MHz during the third heating period. A particular low-frequency reduction appears for X-mode heating at magnetic zenith for the third and fourth heating periods, in the range 1 to 1.7 MHz. Narrow frequency ranges may be automatically removed by the ionosonde software if it detects interference lines, but the depletions in Figure 4-3 are rather wide and show rough edges, not characteristic of software-removed interference lines. This is consistent with the ionograms themselves in Figure 4-2. During the fourth and fifth heating periods there is a significant decrease in signal at frequencies around 4.5 MHz, and a less prominent reduction in slightly lower frequencies, down to about 4.1 MHz.

The frequency range from 3.1 to 3.3 MHz was further analyzed, and a plot of amplitude versus time is shown in Figure 4-4. There is a clear effect during the first three heating periods, where O-mode and X-mode heating are done near 3.16 MHz, respectively. This is seen in both polarizations of the ionosonde signal. The effect of the heater is not as clear in the higher frequency heating, showing that either the heater did not cause as significant a scattering of ionosonde signals, or that the signals that were scattered tended to be weaker (this is likely since the predominantly affected traces are oblique).

34

4.3 March 2006

In March 2006, we joined a spring campaign at HAARP, and further studied the development of the thermal filamentation instability. In the time we had for experiments, we turned the heater on for two 15 minute intervals, and allowed the plasma to relax for 54 minutes between. We transmitted O-mode first and then X-mode heater waves. The peak plasma frequency (foF2) during this experiment was relatively small, and the ionosphere was very weak. Ionogram traces were weak to nonexistent, and during heating disappeared altogether. Absorption fluctuated between .1 and .25 dB during this time.

Figure 4-5 shows skymap data during the heating experiments. Panel (a) shows a skymap before the heater was turned on, and panel (b) is shortly after we began 2.76 MHz O-mode heating, transmitting a vertical beam. Panels (c) and (d) are between the two heating periods, when the ionosphere was relaxing. Then we transmitted 2.76 X-mode heater waves vertically, and panel (e) shows a skymap acquired shortly after this heating began. Finally, panel (f) shows a skymap from after our heating stopped, indicating that the ionosphere again relaxed.

Figure 4-6 shows a plot of total skymap intensity versus time. There is a clear reduction in skymap traces during the two heating periods, with the total signal decreasing by about 30 dB on average. Between the heating periods and after we stopped heating, the ionosonde returns increased to an unperturbed level (between 75 and 80 dB for most of the experiment). One other notable feature is the sudden loss of signal for 10 minutes beginning at 7:23 UT. However, since the signal goes to 0 dB this looks like an instrument artifact as opposed to a significant physical effect.

4.4 Summer 2006

We conducted experiments on August 9, 2006 from 4:20 UT to 7:00 UT. During this campaign we wanted to test our interpretation of summer 2005 data and verify the
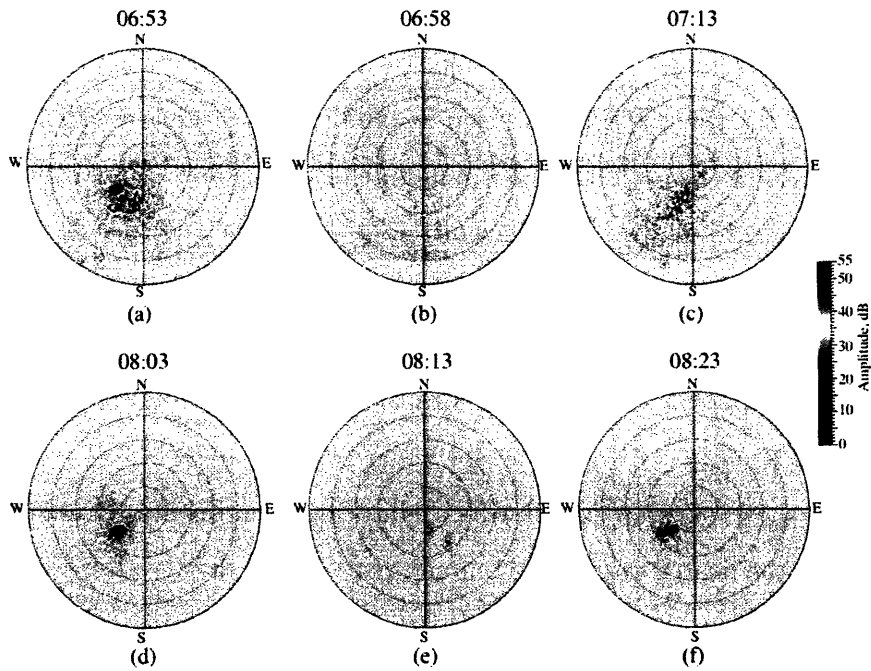
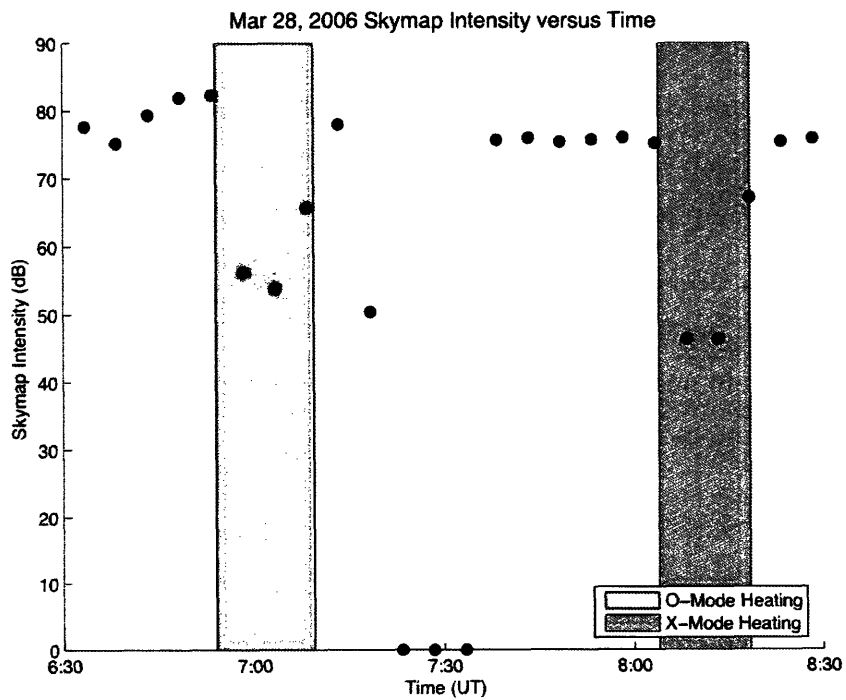Figure 4-5: Representative skymaps from March 28, 2006

Figure 4-6: Total skymap intensity on March 28, 2006

Ionogram Number	Heating
Ionogram 1	3 min. on 2 min. off
Ionogram 2	2 min. off 3 min. on
Ionogram 3	5 min. off
Ionogram 4	5 min. off
Ionogram 5	3 min. on 2 min. off
Ionogram 6	3 min. off 2 min. on
Ionogram 7	3 min. on 2 min. off
Ionogram 8	5 min. off

Table 4.1: Heating Scheme Coinciding with Ionogram Acquisition, August 9, 2006

geometry-dependent effects of heater-induced parallel-plate waveguides on ionosonde signal propagation. We set up a heating scheme that allowed heating and relaxation of the ionosphere for each heater polarization, and also timed the heater operation to coincide with ionogram acquisition. The ionosonde was configured to operate from 1 to 6 MHz, taking one ionogram and one skymap every five minutes. The first three minutes of this cycle were used to record the normal signals comprising an ionogram, while the last two minutes were operated in skymap mode to produce a two-dimensional plot of returned signal direction with either Doppler velocities or signal intensity. We used a repeating cycle of on/off heating timed to coincide with the ionsonde operations as shown in Table 4.1. This cycle took 40 minutes and allowed a variety of ionogram types, some acquired when heating began, some taken after a period of heating, and some taken during relaxation. The 40 minute cycle was repeated four times, two each with O-mode heating and X-mode heating, but the two different types of heating were alternated.

Figure 4-7 shows the absorption during this experiment. The data points were read off the riometer display at the times when ionogram acquisition began, and the error bars show the uncertainty in this reading. Absorption peaked around 1.3 dB at 5:20 UT. From the beginning of the experiment until this peak, the absorption
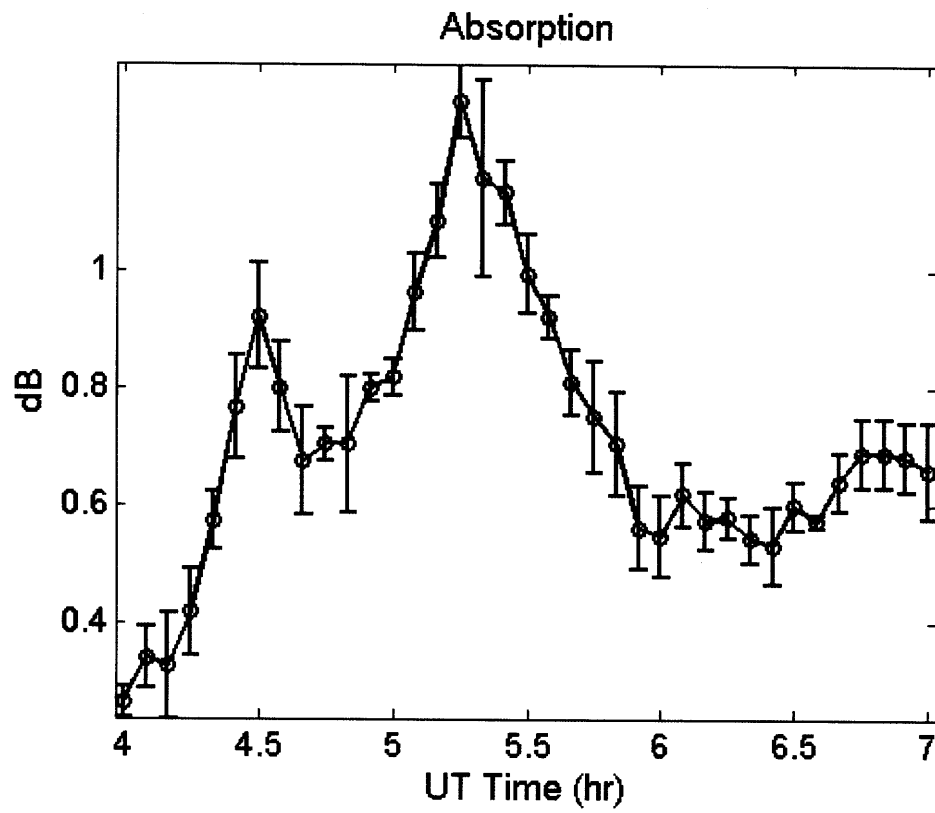
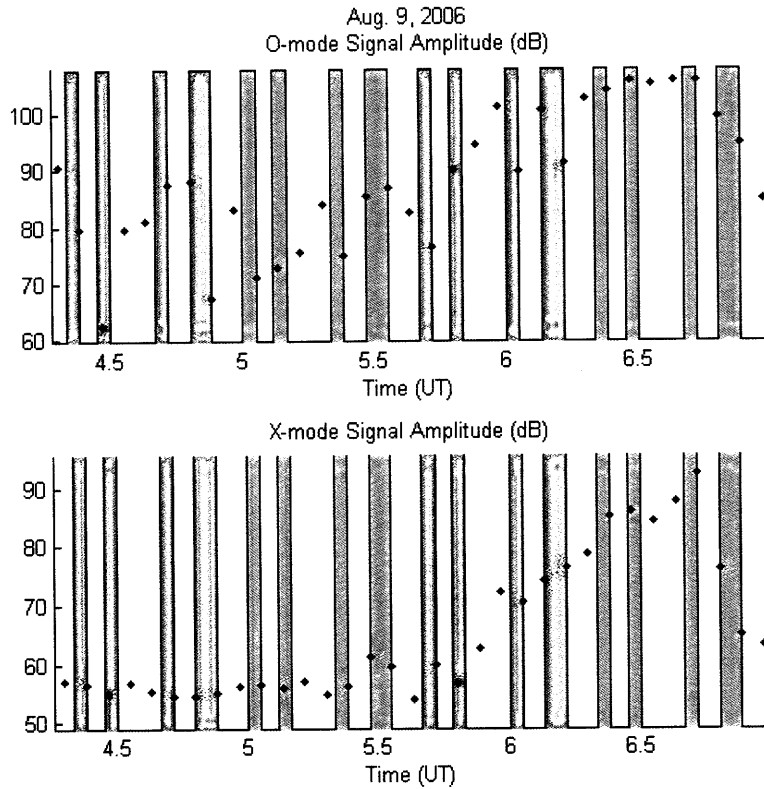Figure 4-7: Absorption on August 9, 2006

Figure 4-8: Ionogram intensity on August 9, 2006

varied between about 0.3 and 1.25 dB. After about 5:45 UT the absorption remained relatively constant until the end of the experiment. In general we would like the absorption to remain constant throughout an experiment, so that variations in ionsonde signal strength are due to processes of interest in the ionosphere. If the absorption varies enough, we may see a signature in the ionosonde that is correlated with this. We originally considered only examining the data after 5:40 UT because of the variations and peak in Figure 4-7. However, referencing the absorption curve during the following ionosonde data analysis shows no clear effect of absorption, which would introduce a systematic effect not related to thermal filamentation.

4.4.1 Correlation of Ionosonde Signals to Heating Scheme

To examine the correlation of ionosonde signal propagation with heater operation, we plot the ionogram intensity versus time in Figure 4-8. Again, O-mode heating is
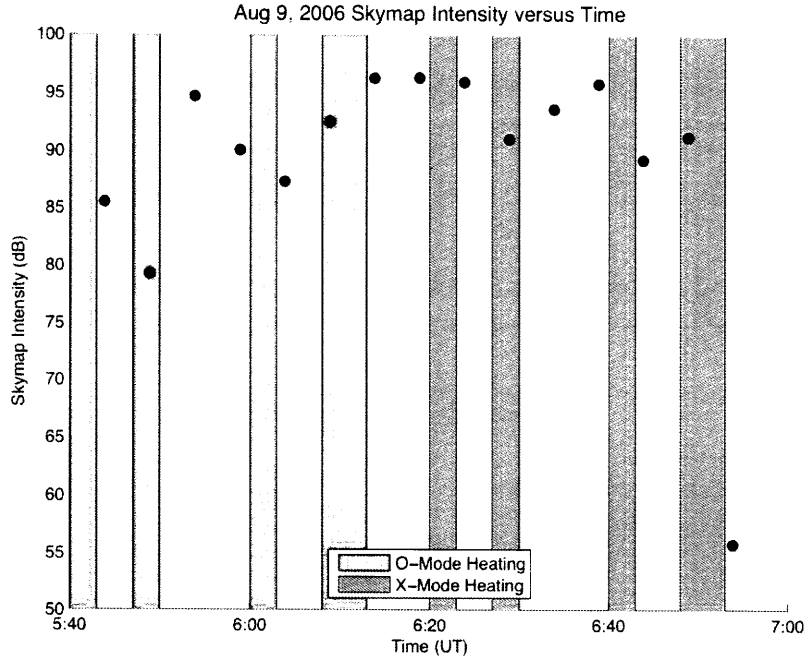
39

Figure 4-9: Skymap intensity on August 9, 2006

indicated by blue regions, and X-mode heating is indicated by orange regions. The X-mode ionosonde signals do not show a significant correlation with the heating scheme, but correlation is seen for the O-mode ionosonde signals. With 32 overall samples, 63% showed decreased signal with heating or increased signal during relaxation, with 31% showing the opposite trend. The remaining samples did not fall clearly in either category. Looking just at the O-mode heating, 81% of the samples demonstrate the expected heater effect, while only 13% show the opposite trend. The X-mode heating is not conclusive, as 44% of the samples show the expected trend, and 50% show the opposite trend.

Figure 4-9 shows the variation in skymap intensity after 5:40 UT. Here there are very few samples with which to study correlation, but the skymap data does corroborate the preceding ionogram analysis. In most cases, the skymap intensity decreases during or immediately after heating, and increases during relaxation. This is seen for 2 of the 7 points during O-mode heating and all 8 points during X-mode heating.

40

Chapter 5

Conclusion

We observed anomalous absorption of ionogram signals during experiments in summer 2005, spring 2006, and summer 2006. We propose a scenario explaining the scattering of ionogram signals due to short-scale heater induced irregularities and large-scale irregularities due to thermal filamentation. We saw a pronounced effect on ionogram traces in summer 2005, with a northward plasma blob affording an opportunity to study obliquely propagating ionosonde signals. In spring 2006, we obtained skymaps to diagnose the effect of thermal filamentation on ionosonde signals during 15 min. heating cycles. In summer 2006, we attempted a correlation study between heater on/off operation and the strength of ionosonde returns. We found an especially convincing effect on O-mode ionosonde signals, which is mostly contributed by O-mode heating.

The generation of large plasma sheets in 1997 Arecibo HF heating experiments has been understood in terms of the thermal filamentation instability [1]. Our recent Gakona ionospheric plasma heating experiments, using a high power HF heating facility and multiple diagnostic instruments, have shed light on the important role of the thermal filamentation instability in generating radio wave-induced plasma turbulence with a broad spectrum of wavelengths, ranging from meter to kilometer scales. In our future Gakona experiments, it would be helpful to have both skymaps and ionograms when the peak plasma density is high and there is a plasma blob, so that the proposed effect of thermal-filamentation instability could be further verified. It is de-

sirable to perform further experiments to investigate this hypothesis, with additional diagnostics such as an All Sky Imager and scintillation measurements.

5.1 Future Work

We will travel in summer 2007 to the URSI conference in Ottawa, Canada, and to the Trieste Workshop in Italy to present these results ([7], [8]). I have received a National Academies of Science fellowship to attend the URSI conference. I am also collaborating with Laura Burton to prepare ionosonde and skymap data for publishing a paper with Prof. Lee entitled, "Generation of Large Plasma Irregularity Sheets by HAARP Heater via Thermal Filamentation Instability," in Geophysical Research Letters [9].

Bibliography

[1] M.C. Lee et. al. Generation of large sheet-like ionospheric plasma irregularities at Arecibo. *GRL*, 25(16):3067–3070, 1998.

[2] Rezy P. et al. Brief Report on HAARP Experiments: Thermal Filamentation, Heater Effect on Spread-F, Cascading PDI's, Whistler-Plasma Interaction. In *Polar Aeronomy and Radio Science Summer School*, Gakona, Alaska, August 2005.

[3] J.A. Cohen and L.M. Burton. Thermal Filamentation. In *Polar Aeronomy and Radio Science Summer School*, Gakona, Alaska, August 2006.

[4] Thomas H. Stix. *Waves in Plasmas*. Springer-Verlag, New York, 1992.

[5] M.C. Lee. Lecture notes. Lecture at ASIS Lab, March 2006.

[6] W.R. Piggott and K. Rawer eds. U.R.S.I. Handbook of Ionogram Interpretation and Reduction, revised. Technical report, World Data Center A, 1978.

[7] J.A. Cohen et al. Diagnoses of Large Plasma Sheets Excited by HF Heater via Thermal Filamentation Instability at Gakona, Alaska. In *URSI North American Radio Science Meeting*, Ottawa, Canada, July 2007. URSI.

[8] J.A. Cohen et al. Diagnoses of Large Plasma Sheets Excited by HF Heater via Thermal Filamentation Instability at Gakona, Alaska. In *Turbulent Mixing and Beyond Workshop*, Trieste, Italy, August 2007. ICTP.

[9] J.A. Cohen et. al. Generation of Large Plasma Irregularity Sheets by HAARP Heater via Thermal Filamentation Instability. *GRL*, 2007.